Research Article | Vol. 33, No. 14 / 14 Jul 2025 / Optics Express 29786
Optics EXPRESS

Design and fabrication of short-period long period gratings for refractive index sensing

RICCARDO FUNARI,[1,2,*] RANA M. ARMAGHAN AYAZ,[1,2] FABRIZIO DI PASQUALE,[1,2] AND CLAUDIO J. OTON[1,2]

[1]Scuola Superiore Sant'Anna, Institute of Mechanical Intelligence, Via G. Moruzzi 1, Pisa 56124, Italy
[2]Department of Excellence in Robotics & AI, Scuola Superiore Sant'Anna, Piazza Martiri della Libertà 33, Pisa 56127, Italy
[*]riccardo.funari@santannapisa.it

Abstract: Fiber optic sensors offer high sensitivity and remote sensing capabilities. This study explores short-period long period gratings (SP-LPGs), fabricated via femtosecond laser, as compact and highly sensitive alternatives to conventional LPGs for refractive index (RI) sensing. Gratings with different periods were modeled and tested using a microfluidic setup. The shortest period ($\Lambda = 13\ \mu m$) showed high sensitivity and RI resolution (1.1×10^{-6} RIU), while the longest provided better linearity. An intermediate-period grating ($\Lambda = 14.25\ \mu m$) offered optimal performance, demonstrating that period selection allows for tailoring sensitivity and linearity. These results make SP-LPGs promising for applications in medical diagnostics and environmental monitoring.

1. Introduction

Fiber optic-based sensors have emerged as a pivotal technology in the field of sensing due to their intrinsic advantages, such as high sensitivity, immunity to electromagnetic interference, and the capability for remote sensing [1–4]. Among the various types of fiber optic sensors, Fiber Bragg Gratings (FBGs) [5] and Long Period Gratings (LPGs) [6–8] stand out due to their distinct operational principles and wide-ranging applications. These sensors are fabricated by introducing a periodic change in the refractive index (RI) in the core of an optical fiber.

Standard FBGs [4,5] typically work in reflection mode on the first order, which requires a period of $\Lambda \approx 530$ nm for light in the 1550 nm wavelength range. In these gratings, light never leaves the core region, so these sensors only respond to parameters affecting the fiber core, such as temperature or strain, but not to chemical or physical changes at the surface of the cladding. In order to have sensitivity at the surface of the fiber, the cladding must be either thinned (by fiber tapering or side lapping) [9,10], or the grating must excite so-called cladding modes, in which light couples out of the core reaching the surface of the fiber to interact with the liquid. By changing the period of the grating, cladding modes can be excited in co-propagation or counter-propagation directions [11,12]. However, in counter-propagation, the spectral separation between cladding mode peaks is very small, making them difficult to distinguish and track. In contrast, in co-propagation, the cladding mode peaks are well separated, and the required grating periods are much longer than those of standard FBGs, ranging between 12 μm and 1 mm [13]. Due to their long periods, these gratings are referred to as LPGs.

LPGs are characterized by drops in their transmission spectrum which are visible as negative peaks, where each peak corresponds to a cladding mode or family of modes. When the external RI changes, these peaks shift because of the interaction of the evanescent field of the cladding mode with the liquid. Tracking these shifts can measure RI variations, which can be used to develop a chemical sensor if the fiber surface is functionalized with a specific receptor.

LPGs have been studied for many years to measure various parameters, including temperature [14–16], strain [17,18], bending [19,20], torsion [21], and especially the surrounding RI

#566073 https://doi.org/10.1364/OE.566073
Journal © 2025 Received 28 Apr 2025; revised 27 May 2025; accepted 29 May 2025; published 7 Jul 2025

Optics EXPRESS

[22–24]. Consequently, LPGs have found widespread application in diverse sensing fields such as physical [25,26], chemical [27], and biological [2,28–31] sensing. However, there are several issues associated with LPG technology. One of the main disadvantages is their sensitivity to environmental perturbations such as temperature and strain, which can lead to cross-sensitivity issues. To mitigate this, careful design and packaging are required to isolate the RI sensing from other influences. Another disadvantage of LPGs comes from their long periods, which require much longer grating lengths than standard FBGs to generate narrow peaks. Most commonly, the periods used in the literature are those that excite the most confined cladding modes, requiring lengths greater than 100 μm [32–34]. These gratings typically extend over several centimeters to produce narrow transmission peaks. However, such long gratings are difficult to use in applications where a compact sensor is needed, or when the homogeneity cannot be guaranteed along such long lengths.

For these reasons, Short-Period Long Period Gratings (SP-LPGs) [32,35–38] offer several enhanced characteristics over their conventional counterparts. Table 1 compares the SP-LPGs investigated in this study with other SP-LPGs and standard LPGs, highlighting key characteristics such as grating length, period length, and RI sensitivity.

Table 1. Comparison of the SP-LPGs described in this study with similar devices and LPGs. SP-LPGs offer a shorter grating length and higher RI sensitivity than conventional LPGs. Additionally, compared to similar grating-based sensors, the devices presented in this study demonstrate good RI sensitivities in the near-IR region, a wavelength range of particular interest for sensing and biosensing applications [42].

	Grating length (mm)	Period Length (μm)	RI Sensitivity (nm/RIU)	RI Range (RIU)	Fabrication Technique	Real time measurement (Y/N)	Ref.
LPG	4	374	N/A	N/A	CO_2 laser	N/A	[39]
	20	80, 150, 300	124.5, 143.4, 131.8	1.33-1.3833	fs laser	N	[32]
	10	100	175.84 (Average)	1.3381-1.3763	fs laser	N	[33]
	37	530	87 (Average)	approx. 1.33-1.39	CO_2 laser	N	[34]
SP-LPG	3	40	189.8	1.3315-1.3845	fs laser	N	[35]
	N/A	25	312.5 (Average)	1.315-1.395	UV laser	N	[38]
	12.5	25	291.5 (Average)	1.33-1.39	fs laser	N	[36]
	2.1	30	N/A	N/A	fs laser	N	[37]
	2.4	30	128	1.333-1.34	fs laser	Y	[40]
	3	30	N/A	N/A	fs laser	N	[41]
	4	**13, 14.25, 50**	**294, 198, 117**	**1.318-1.322**	**fs laser**	**Y**	**Present work**

Due to their shorter period length (in the range 10–50 μm), SP-LPGs have a compact size, with the grating length typically requiring just a few mm. This compactness enables their integration into smaller and more confined spaces, making them suitable for applications where space is constrained. Additionally, SP-LPGs can provide higher sensitivity to RI changes due to the increased interaction of the evanescent field with the surrounding medium over a shorter overall length. This increased sensitivity is particularly beneficial in biochemical sensing, where detecting minute RI changes is crucial. In medical diagnostics, their compact size and high sensitivity make them ideal for integration into minimally invasive devices, such as intravenous catheters, for real-time monitoring of biochemical markers [2,43]. In environmental monitoring, SP-LPGs can be deployed in remote or confined locations to detect changes in water quality or

Optics EXPRESS

atmospheric conditions [44,45]. Furthermore, in industrial process control, SP-LPGs can be used for precise monitoring of fluid compositions and other critical parameters [46]. The ongoing advancements in fabrication techniques and design optimization continue to expand the potential applications and improve the performance of SP-LPGs, making them a promising tool in the field of RI sensing.

In this work, we demonstrate femtosecond-written SP-LPGs with a fixed length of 4 mm, and three different periods between 13 and 50 μm. These periods excite cladding modes that are weak in the core, but can still produce well contrasted (>10 dB) and narrow (FWHM<5 nm) peaks. These peaks are interleaved families of odd and even L cladding modes, which are well reproduced by the simulations, and theoretically discussed for the first time to the best of our knowledge. These results highlight how our femtosecond-written SP-LPGs compare favorably with recent state-of-the-art LPG-based sensors. As summarized in Table 1, our devices uniquely combine high refractive index sensitivity (up to 294 nm/RIU), short grating length (as small as 4 mm), and tunable spectral response. Such compactness facilitates integration in constrained environments while maintaining high performance. Moreover, the ability to tailor the grating period allows optimization of sensitivity, dynamic range, and resolution depending on the application. Compared to recently reported SP-LPGs fabricated via femtosecond or UV laser techniques, our approach demonstrates superior or comparable performance in both sensitivity and footprint, emphasizing the strength of our design-driven fabrication strategy.

We integrated the fiber optic sensor in a microfluidic chip and monitored the peak positions versus RI changes by exposing the fiber to different concentrations of glycerol in water, showing excellent agreement with theoretical predictions. In particular, the device with the shortest period length (Λ = 13 μm) offers the highest RI sensitivity, but it also has the shortest detection range before reaching saturation. On the other hand, the grating with the longest period length (Λ = 50 μm) provides greater linearity and lower sensitivity, although the limited number of periods in this case results in a low signal-to-noise ratio (S/N ratio), leading to reduced resolution. Finally, the SP-LPGs with an intermediate period length (Λ = 14.25 μm) offers the best compromise between sensitivity and linearity, providing optimal flexibility for applications requiring surface functionalization. This design-driven approach to tailoring optical response by tuning the period length represents the main novelty of our work and fills a current gap in the systematic optimization of SP-LPG parameters. In these SP-LPGs, we measured unprecedented levels of RI resolution down to 1.1×10^{-6} RIU. These results demonstrate that our SP-LPGs are versatile and robust sensing devices that can be designed to fine-tune their RI sensitivity, linear range, and resolution according to the specific needs of the final application.

2. Design and model

2.1. Optical fiber model

In standard FBGs, the fiber can be modeled as a core surrounded by a cladding. Since the index contrast is low, the solutions can be calculated using linearly-polarized (LP) modes, which are a good approximation of the actual EH modes, which are the exact solutions of the three components of the electric and magnetic fields. When cladding modes are excited, the simulation requires considering 3 layers: the core, the cladding, and the surrounding medium, which can be air, or the liquid where the fiber is immersed. In addition, the index contrast between the fiber and the surrounding medium is not small, thus the LP mode approximation does not provide a precise model. For these reasons we calculated the EH cladding modes by using a 4×4 transfer matrix model applied to a 3-layer optical fiber.

The procedure is described in detail in [47], and we implemented it in python code with the modifications proposed in [48] for more efficient calculation. Using this method, the effective indices of the cladding modes were found by first applying the dispersion equation to a broad range of effective indices to look for sign changes, and then each zero was found using Brent's

Optics EXPRESS

method from the bracket points. The optical model used for the silica glass cladding is from [49], with a refractive index of 1.444 at 1550 nm and a dispersion calculated using Sellmeier equation. The index of the core was calculated by increasing the index of the cladding assuming a numerical aperture of 0.124 (which gave the best fit with the experimental positions of the peaks, and was also very close to the value indicated in the specifications of the fiber). The model for water is from [50], which yields a refractive index of 1.318 at 1550 nm, and the dispersion equation from a third-order polynomial fit of the data between 1 and 2 μm wavelength. The diameters of the core and cladding layers were set to 8.2 and 125 μm obtained from the specifications of the SMF-28 fiber.

We computed the cladding modes applying cylindrical symmetry:

$$\begin{aligned}\mathbf{E}(r,\theta,z) &= \mathbf{E}(r)exp(jL\theta + jk_0 n_{eff} z - j\omega t)\\ \mathbf{H}(r,\theta,z) &= \mathbf{H}(r)exp(jL\theta + jk_0 n_{eff} z - j\omega t)\end{aligned} \tag{1}$$

where $\mathbf{E}$ includes the three cylindrical components of the electric field and $\mathbf{H}$, of the magnetic field; k_0 is the vacuum wavenumber $2\pi/\lambda$; n_{eff} the effective index of the mode; and L is the integer that determines the azimutal dependence of the mode in θ.

The method allows to calculate both the fundamental core mode HE_{11}, and all the cladding modes. It is worth noting that since we are using cylindrical components of the fields, the core mode has a value $L = 1$, unlike in LP modes where the fundamental mode has $L = 0$.

On the other hand, the grating can be simulated as a periodic perturbation of the RI with a period Λ. A significant coupling to a cladding mode requires phase matching condition, which is determined by this equation:

$$\lambda_{\text{peak}} = (n_{eff}^{(\text{core})} - n_{eff}^{(\text{clad})})\Lambda \tag{2}$$

where $n_{eff}^{(\text{core})}$ is the effective index of the core mode, while $n_{eff}^{(\text{clad})}$ is the effective index of the cladding mode. In order to find the expected resonance peaks for a given period, a line that follows this equation can be traced, and whenever there is a crossing with the cladding mode lines versus wavelength, it means coupling can occur and a dark peak in transmission can be observed.

In order to find the expected resonance wavelengths, we calculated the cladding modes within a wavelength range between 1450 and 1650 nm. A standard SMF fiber surrounded by water has thousands of cladding modes, but in our case we are only interested in modes with significant field in the core region, which corresponds to the first few integer values of L. In Fig. 1 we show the dispersion curves of all the cladding modes for L between 0 and 5. The core mode is shown at the top part as a blue line, while the cladding modes are in the region between the RI of the cladding and the one of water. The modes having n_{eff} close to the index of the cladding are the most confined cladding modes, which are the ones excited by most typical LPGs with long periods. On the other hand, grating periods between 12 and 50 μm excite higher-order cladding modes, which tend to cluster according to L parity, as shown in the figure. This means that we expect to find alternating families of peaks in transmission, corresponding to odd and even L cladding modes. In particular, in Fig. 1(e) we show the mode profiles of all the modes with L = 0, 2, 4 which contribute to the central LPG peak at 1555 nm expected with a grating period of 14.25 μm. The indicated indices follow the nomenclature of Ref. [51], where L was defined in Eq. (1) and ν denotes the cladding mode position in decreasing order of effective index starting at 1, which corresponds to values between 84 and 88 in this effective index region. In that panel it is clear that the field intensity in the central part of the core region decreases with increasing L, which is why we did not consider L values higher than 5 in our simulation. The list of cladding modes excitable with periods 50, 14.25 and 13 μm are shown in Table S1 in Supplement 1.

The core mode (LP_{01} or HE_{11}) has $L = 1$ in cylindrical coordinates; this implies that if the grating RI perturbation had cylindrical symmetry, only cladding modes with the same value of L could be excited [51]. If the grating perturbation was not cylindrically symmetric, but

Optics EXPRESS

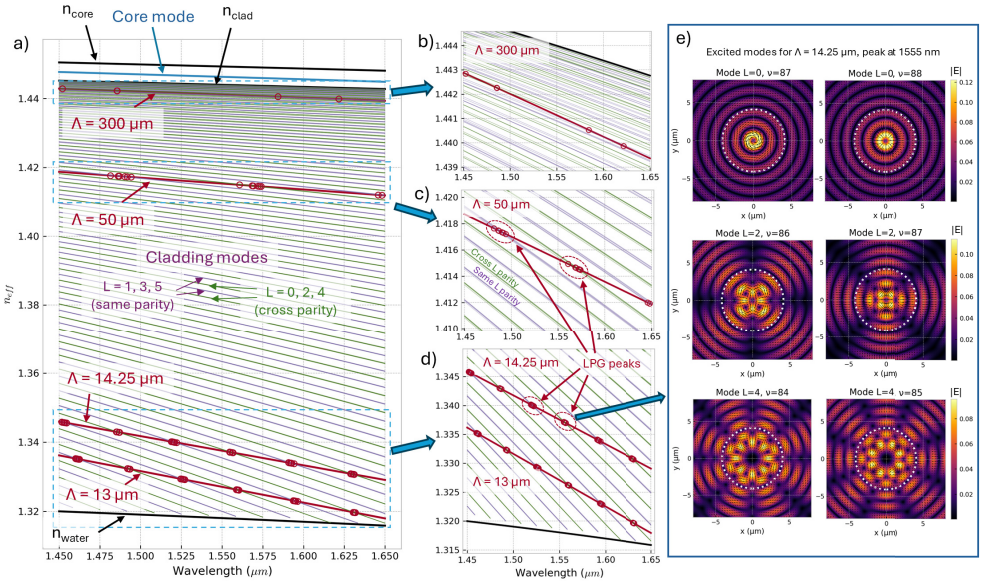

Fig. 1. Calculated LPG modes for a standard SMF-28 fiber surrounded by water. The red lines show the phase-matching conditions for different grating periods, in particular 13, 14.25, 50 and 300 μm. The solid cyan line is the core mode ($L = 1$), while the violet and green lines show all cladding modes for L values between 0 and 5, grouped by L parity, where same-L-parity modes ($L = 1, 3, 5$) are violet, and cross-L-parity modes ($L = 0, 2, 4$) are green. The crossings between the LPG modes and the phase-matching red lines mark the peaks in the transmission spectra. a) Full effective index range; b) Zoom around a typical LPG with 300 μm period; c) Zoom around an LPG of 50 μm period; d) zoom around periods 13 and 14.25 μm, which can excite modes that are closest to lossy modes; e) Mode profiles corresponding to the cladding modes excited with a period of 14.25 μm at 1555 nm wavelength. The color represents the electric field modulus, the arrow indicates the electric field direction, and the dotted white circles mark the core-cladding interface.

had inversion symmetry (for example an elliptical shape centered at the fiber axis), only modes with the same parity (odd L values) could be excited. Finally, if the grating perturbation had no symmetry (for example if there was an offset in the inscription), any mode parity could be excited. For this reason, we classified the cladding modes as *same-parity* if the L parity is odd, and *cross-parity* if the L parity is even. If the perturbation size is much smaller than the core (as is the case in fs-written gratings), the relative strengths of *same* and *cross* parity are expected to be strongly dependent on the offset of the femtosecond inscription with respect to the fiber axis. We observed mathematically and experimentally that even small offsets (smaller that 1 μm) can strongly couple cross-parity modes, therefore in transmission we expect to observe both peak families that alternate spectrally in an interleaved series with different peak depths. In the next section we will see that this is indeed the case, as femtosecond laser writing induces very small-size index perturbations, which makes them difficult to perfectly align to the fiber axis. This is an important difference with respect to traditional UV-written LPGs, where the index perturbation is much larger, which means that only cladding modes with $L = 1$ can be excited in this kind of gratings [51].

Optics EXPRESS

2.2. Sensitivity calculations

In order to predict the sensitivity of the LPG as a RI sensor, we recalculated all the modes applying a small RI variation in the liquid, calculating the resonance shift, and normalizing the shift with the change of the RI applied. The results of this calculation are shown in Fig. 2. We show the sensitivities of all the resonant cladding modes for L between 0 and 5, and we grouped them by parity as all modes with the same parity are expected to overlap on a single peak. As expected, grating periods exciting the highest-order cladding modes (with periods 13 and 14.25 μm) show considerably higher sensitivity than longer periods, because of the increased evanescent field of these modes in the liquid. Since each peak is actually the combination of several modes, even though each mode has a slightly different sensitivity, for each peak we expect to observe an average of all the sensitivities that are contributing to that peak (grouped within the ellipses in Fig. 2).

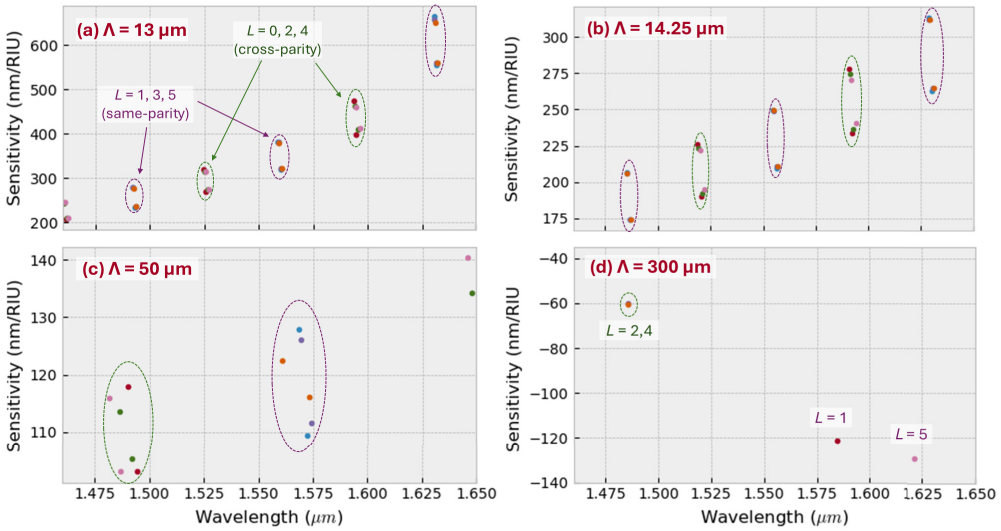

Fig. 2. Calculated sensitivities to RI change around the index of water, for L values between 0 and 5, and for different grating periods: (a) 13 μm, (b) 14.25 μm, (c) 50 μm, (d) 300 μm. Resonances have been grouped by L parity, using violet color for odd L (same-parity) and green for even L (cross-parity).

It is also worth noting that the simulation of the longest period (300 μm, shown in Fig. 2(d)) shows a change in sign in sensitivity, which predicts a blue shift instead of a red shift when the RI increases. This is a well-known feature of LPGs with long periods, and is due to the switch of the slopes of the phase-matching line and the cladding mode lines around the turn-around point (TAP), which occurs at periods around 100 μm for this type of fiber and spectral range.

For deciding the best grating period for a liquid sensor, one must consider not only the sensitivity value, but also the RI range of linearity and the width and depth of the peak. If one chooses a period that excites modes very close to lossy modes (represented by period 13 μm in our case), the sensitivity can potentially be very high (up to 600 nm/RIU), but a large change of RI will make the peak disappear as it turns into a lossy mode. On the other hand, for a period of 50 μm, a much wider peak is expected due to a smaller number of periods (considering a fixed grating length) and also because the modes within the family are more spectrally spread as shown in Fig. 2(c). A good trade-off could be a period of 14.25 μm, shown in Fig. 2(b), which has a good sensitivity (200 to 300 nm/RIU), low spectral spread of the mode family (about 2.5 nm), and a RI range close to 0.02 as shown in Fig. 1(d). In addition, limiting the sensor length to 4

Optics EXPRESS

mm, that period would allow inscribing 280 periods, which can potentially reduce the bandwidth of the peaks to around 5 nm in the 1550 nm spectral band, unlike for much longer periods where the peaks are expected to widen dramatically if the LPG length is kept fixed. For these reasons, the periods chosen for this experimental study were the first three simulated cases (13, 14.25 and 50 μm).

3. Experimental section

3.1. LPG fabrication setup

In this study, SP-LPGs are fabricated on standard single-mode fibers (SMF-28). The gratings are inscribed using a femtosecond laser (Spectra Physics Spirit One 1040 8 SHG) on a short section of the fiber that has been mechanically stripped and carefully cleaned with IPA.

Before the writing process, the stripped section of the fiber is placed on a glass slide and immersed in index-matching liquid (Cargille Laboratories). A cover slip is then positioned over the fiber to prevent focal distortion or lensing effects that could arise from the curved surface of the fiber. The entire assembly, containing the stripped SMF, is mounted on a computer-controlled 3D translation stage (Newport M-37 series). During the LPG fabrication process, the stage moves parallel to the fiber axis at a speed of 99.913 μm/s while the laser is operated with an external function generator (Agilent, 33250A) providing square wave with 50% duty cycle to inscribe the grating with the desired Λ into the fiber core. The laser operates at a wavelength of 520 nm, with a repetition rate of 200 kHz, and a pulse duration of approximately 350 fs, which was attenuated to reach an average power of 3.5 mW. The laser pulses are focused onto the optical fiber through a 40× objective (ZEISS EC Plan-Neofluar 40×, NA 0.75). Figure 3(a) illustrates the schematic of the LPG writing setup.

After the manufacturing process, the SMF with the inscribed LPG is removed from the stage and cleaned with IPA to eliminate any residual index-matching liquid before recording the transmission spectrum. This process is performed to fabricate SP-LPGs with period lengths of 13, 14.25, and 50 μm on separate SMFs. The resulting grating patterns and transmission spectra can be observed in Figs. 3(b), (c), (d) and Figs. 3(e), (f), (g), respectively. It is important to note that the red and blue lines in the recorded spectra of the SP-LPGs (Pol. 1 and Pol. 2 in Fig. 3(e, f, g)) correspond to two different orthogonal input light polarizations, while the green and purple areas indicate the spectral band where the same-L-parity and cross-L-parity modes are clustered, respectively. A good agreement of the experimental and calculated spectral bands was observed (the periods used for the simulation of the 13 μm and 14.25 μm were the nominal ones, while for the 50 μm we used 50.8 μm to better align the bands with the experimental plot). It is worth noting that in some cases the cross-parity peaks are deeper than the same-parity ones, while the theory predicts that if the index perturbation had inversion symmetry, the cross-parity peaks would not be excited at all. Since we are using a fs laser to write the grating lines, the perturbation points are much smaller than the core, thus offsets with respect to the fiber axis are expected. In presence of a lateral offset, the excitation of cross-parity modes is not only possible but can even be higher that the same-parity modes, as shown by our experiments. In any case, the key feature required to have a clean refractive index measurement is at least a peak with a good extinction, narrow width, and easy to identify in the spectrum, and these features are observed in both cases (a) and (b), while the broad peak observed in (c) is expected to show a more noisy response.

To evaluate the reproducibility of our fabrication process, we analyzed the transmission spectra collected in air of multiple SP-LPGs from different fabrication batches. An example for the 13 μm period length is shown in Supplement 1 (Fig. S1), where the peak pattern remains consistent across all spectra, demonstrating that the wavelength separation between consecutive resonant dips of the same family (Free Spectral Range, FSR) is identical for each grating. This confirms the reliability and repeatability of our femtosecond laser fabrication approach, thus ensuring consistent performance across multiple fabricated devices.

Optics EXPRESS

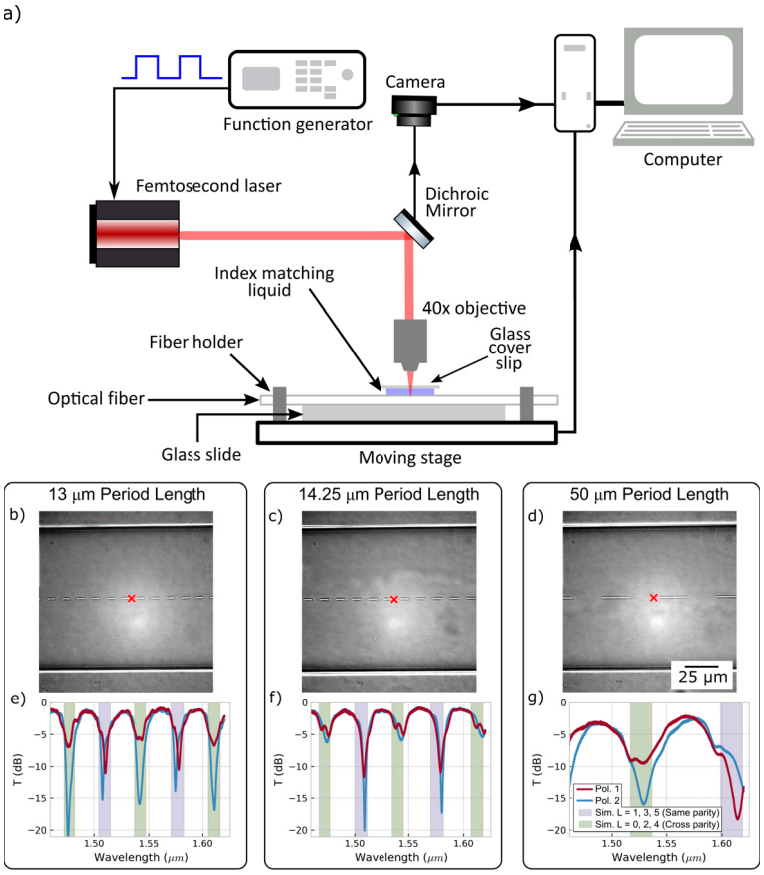

Fig. 3. (a) Schematic representation of the setup used to fabricate the SP-LPGs. Representative microscopic images of SP-LPGs with Λ of 13 μm, 14.25 μm, and 50 μm are shown in (b), (c), and (d), respectively. These images are captured using the microscope integrated into the fabrication setup. The corresponding transmission spectra collected in air for the three period lengths are presented in (e), (f), and (g), with the legend in panel (g) indicating the spectra corresponding to the two polarizations, while the green and purple areas highlighting the same-L-parity and cross-L-parity modes, respectively.

3.2. Materials and chemicals

Polydimethylsiloxane (PDMS) (SYLGARD 184 Silicone Elastomer Kit) is purchased from Dow Corning. Double-coated adhesive polyolefin foam tape (NITTO, 5704LE) is kindly provided by NITTO, Italy. Glycerol (Sigma Aldrich, G7757), isopropanol (IPA, RS Italy, 187-6955), and deionized water (DI water) are used for the RI sensitivity measurements and sample preparation. To determine the refractive index (RI) of the glycerol-water mixtures used in this study, we employed a third-degree polynomial model following the approach of Saunders et al. [52]. The RI of the mixture (n_{sol}) was calculated as a function of the glycerol weight fraction (w) using the equation:

$$n_{\mathrm{sol}} = Aw^3 + Bw^2 + Cw + D \tag{3}$$

where the coefficients are defined as $A = -0.0215$, $B = -0.0512$, $C = 0.111$, and $D = 1.318$, the latter corresponding to the RI of water at 1550 nm. Since the RI of glycerol-water mixtures exhibits a predictable spectral trend, we extended the model to different wavelength ranges by

Optics EXPRESS

adjusting D as an offset, using reference values from [50]. This approach ensures accurate determination of RI values across the relevant spectral region.

3.3. Optomicrofluidic chip and interrogation platform

The schematics illustrating the chip assembly and a snapshot of the optomicrofluidic platform are provided in Supplement 1 (Fig. S2). The SP-LPGs inscribed on the optical fiber (III in Fig. S2a) is placed on standard glass slide (IV in Fig. S2a), and is subsequently bonded to a 3 mm thick polydimethylsiloxane (PDMS) slab (I in Fig. S2a) using a 350 μm thick double-coated adhesive polyolefin foam tape (NITTO, 5704LE, II in Fig. S2a). The tape is cut into 3 cm $\times$ 2 cm pieces using a scalpel, which is also used to remove an S-shaped area from the middle of the tape, creating the microfluidic channel. The long section of the channel is approximately 1.5 cm in length and 1.5 mm in width, designed to host the SP-LPGs. The short arms of the channel, each approximately 6.5 mm long, are designed to connect the device to the inlet and outlet channels. The only precaution in this approach is selecting a double-sided tape with a thickness larger than the diameter of the optical fiber (i.e., 125 μm). The PDMS slab (I in Fig. S2a) measures 3 cm $\times$ 2 cm $\times$ 3 mm (length $\times$ width $\times$ height). Holes with a diameter of 2.5 mm are punched in the PDMS slab for sample delivery using 0.7 mm ID Tygon tubing. The final chip assembly is shown schematically in Fig. S2b and as a snapshot in Fig. S2c.

The assembled chip is then mounted as illustrated in the schematic in Fig. 4. The chip (a, with b showing the SP-LPGs enclosed in the microfluidic channel and c a snapshot of the assembled chip) is connected to a Single Syringe Pump (NE-1000 New Era Pump Systems, Inc.) (d), operated at a flow rate of 100 μL/min, and a valve MUX Microfluidic Flow Switch Distributor (Elveflow) (e) to facilitate switching between different samples (f) (i.e., DI water and glycerol aqueous solutions ranging from 0.25% to 10% volume concentration).

Notably, these experimental conditions, particularly the flow rate, ensure fast and reliable results. A flow rate of 100 μL/min is reasonable for experiments designed to characterize the RI sensitivity of the sensing device, as these primarily focus on exposing the sensing surface to solutions with varying RIs. This is evident from the sensorgrams in Fig. 6, where the peak position stabilizes promptly after introducing a new sample into the microfluidic channel containing the fiber optic. While this configuration is effective for RI sensitivity measurements, lower flow rates are recommended for chemical sensing experiments involving molecular recognition events [53,54].

Finally, the fiber with the fabricated SP-LPGs is connected to an optical interrogator (Luna Technologies Hyperion si155) (j) and a polarization controller (g). As shown in the schematic of the experimental setup in Fig. 4, two channels of the interrogator are connected to work in transmission instead of reflection by using an isolator. Unpolarized light from Ch. 1 of the interrogator passes through the SP-LPGs housed within the fluidic chip assembly (a) and reaches the polarization controller (g). The light then passes through an isolator (i) to prevent back reflections coming from Ch. 2 and Ch. 3, and is subsequently split into two polarized beams using a polarization beam splitter (PBS) (i). The purpose of the polarization controller is to align the polarizations of the grating to the polarizations of the PBS, to be able to measure them independently and simultaneously using two channels. The optical signals from the two outputs of the PBS are then directed into Ch. 2 and Ch. 3 of the interrogator, where they are recorded, further processed, and displayed on the connected computer (k). The sample rate of the acquisition was 100 samples/s.

Optics EXPRESS

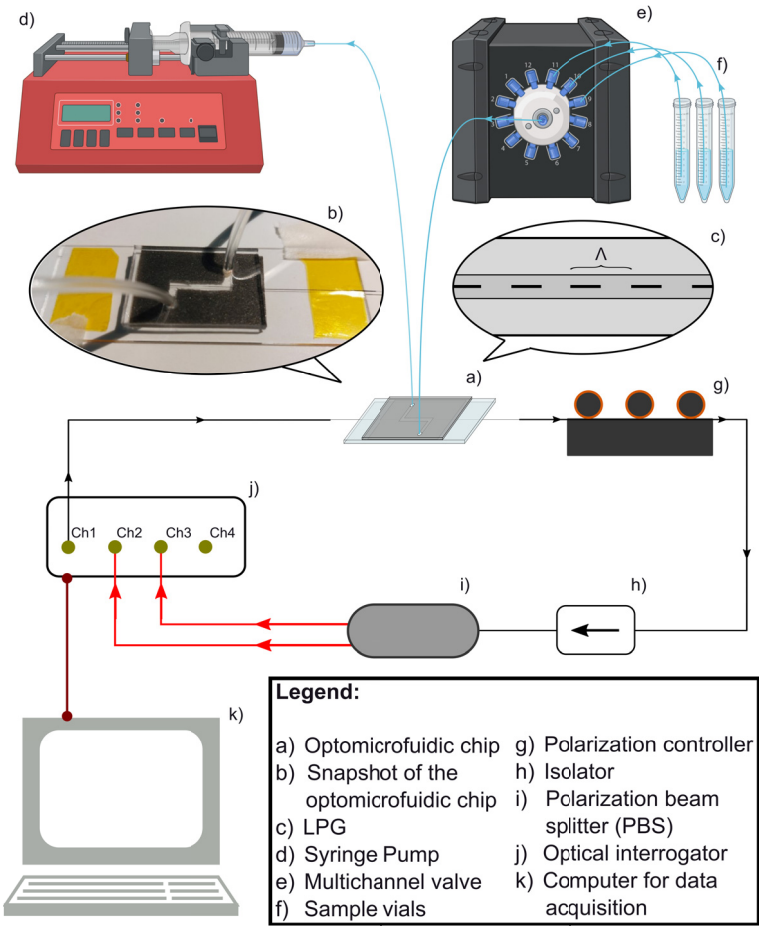

Fig. 4. Schematic describing the experimental setup, including the optomicrofluidic chip (a), (b) and (c), the microfluidic components (d)-(f) and the optical elements (g)-(k) (part of this figure was generated with BioRender.com).

4. Results and discussion

4.1. RI sensitivity characterization of the SP-LPGs

To determine the RI sensitivity of the three SP-LPGs, the gratings are exposed to solutions with varying RI (i.e., water and water/glycerol mixtures with concentrations ranging from 0.25% to 10% v/v) [52]. This is achieved by enclosing the portion of the optical fiber containing the grating within a microfluidic chip, as depicted in Fig. S2. Once the chip is connected to the other microfluidic components and the fiber is integrated into the optical setup (as shown in Fig. 4), the SP-LPGs is initially exposed to DI water, which serves as the baseline for the measurements. The interrogator software (ENLIGHT 1.18.8.0) is employed to monitor real-time changes in the transmission spectra, allowing us to track shifts in the transmission peaks.

While the top panels in Fig. 5(a), (b), and (c) display the complete transmission spectra for the three SP-LPGs (with period lengths of 13, 14.25, and 50 μm, respectively), the bottom panels provide a zoomed-in view of the most intense peak for each grating. It is important to note that due to the limited number of periods in such a short grating (4 mm in length), the spectrum of the 50 μm SP-LPGs is the noisiest among the conditions studied, which significantly limits its RI

Optics EXPRESS

resolution. Initially, DI water is conveyed through the microfluidic chip for 300 s, followed by the introduction of the first glycerol solution (0.25% v/v), which is kept flowing for an additional 300 s. When the glycerol sample reaches the grating, it causes a significant change in the RI of the surrounding medium, resulting in the red shift of the transmission peaks of the SP-LPGs. This shift is clearly visible in Fig. 5(d), (e), and (f), as well as in Fig. 6, which shows the wavelength shift of each SP-LPGs peak over time. After 300 s, the microfluidic circuit was flushed with DI water, causing the spectra to revert to their initial state. This procedure was repeated with six different glycerol solutions (0.25, 0.5, 1, 2, 5, and 10% v/v), producing the spectra and sensorgrams presented in Figs. 5 and 6. It is also worth noticing that, especially in the 13 μm period case, the highest concentration resulted in a significant decrease of the peak contrast and an increase in its width. This is due to the transition from cladding mode to lossy mode that occurs for the LPG with the shortest period, which confirms the fact that the shortest period provides the highest sensitivity but the lowest RI range, as we mentioned in the previous section.

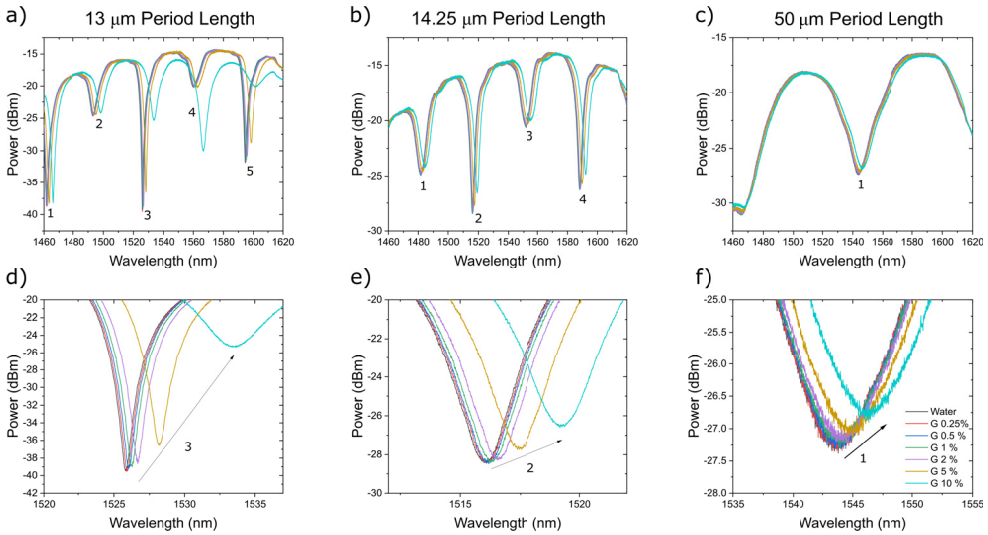

Fig. 5. (a), (b), and (c) Transmission spectra of the three SP-LPGs exposed to aqueous solutions with different refractive indices (RI), prepared using water and water/glycerol mixtures with varying concentrations from 0.25% to 10% v/v. (d), (e), and (f) Zoomed-in views of the strongest peaks for the three LPGs. The black arrow indicates the red shift in the transmission peak as the RI of the solution increases. The legend in panel (f) applies to the glycerol samples used in all experiments.

The peak shifts for each SP-LPGs are used to calculate their RI sensitivity. The wavelength shifts resulting from the exposure of the SP-LPGs to different water/glycerol samples are plotted against the corresponding RI in Fig. 7. In Figs. 7(a), (b), and (c) it is evident that the responses recorded at 5% and 10% glycerol concentrations are significantly nonlinear for both the 13 and 14.25 μm SP-LPGs, whereas the 50 μm SP-LPGs exhibits a linear response across the entire RI range investigated. Since all SP-LPGs display a linear response to the RI of the samples up to 2% glycerol, the RI sensitivities are calculated by linear regression of the peak shifts in this RI range, as shown in Figs. 7(d), (e), and (f). The RI sensitivity values resulting from this analysis are reported in Table 2. The observed superlinear behavior beyond 2% glycerol concentration for (a) and (b) is also predicted from simulations and previously reported in other works [38].

Finally, we evaluate the RI resolution of the three SP-LPGs by measuring the fluctuations in the position of their strongest transmission peaks while flowing DI water into the microfluidic chip at a flow rate of 100 μL/min for 150 s. Figure S3(a) in Supplement 1 shows the overlapped

Optics EXPRESS

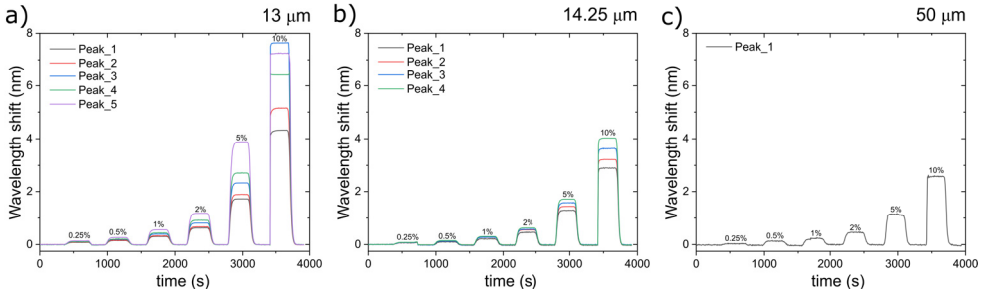

Fig. 6. Representative sensorgrams showing the shift in the LPG peak position upon exposure to glycerol solutions of varying concentrations (v/v). After each incubation with the glycerol sample (as indicated in the graphs), the microfluidic chip is purged with DI water, resulting in the peak returning to its original position. Panels (a), (b), and (c) correspond to the 13 μm, 14.25 μm, and 50 μm SP-LPGs, respectively, with the different curves representing the peaks highlighted in Fig. 5.

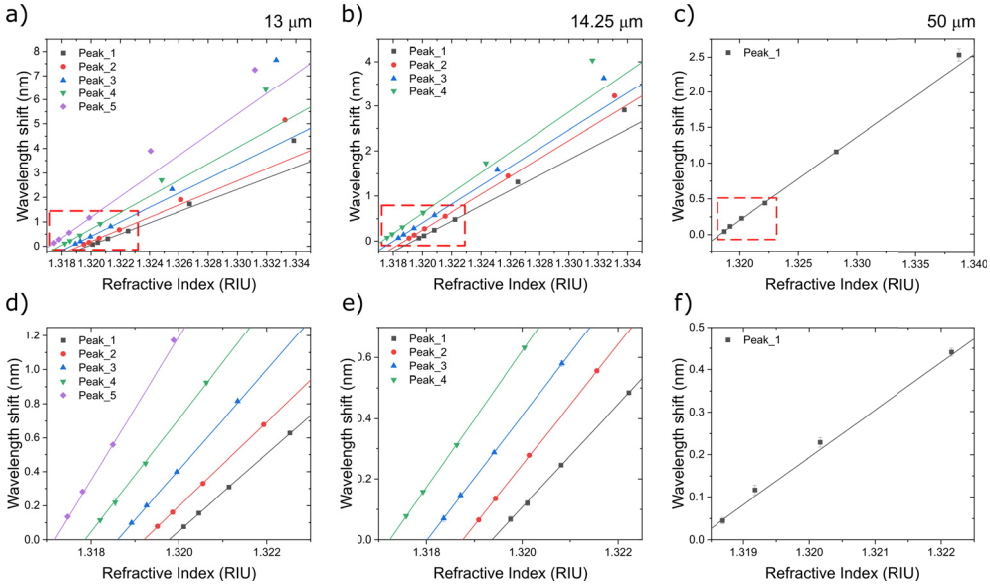

Fig. 7. Peak shifts for each SP-LPGs versus the RI of the corresponding water/glycerol mixture. Panels (a), (b), and (c) show that the response recorded at 5% and 10% glycerol is nonlinear for both the 13 and 14.25 μm SP-LPGs, while the 50 μm SP-LPGs exhibits a linear response across the entire range of RI investigated. The red dashed squares highlight the range shown in panels (d), (e), and (f), where it is evident that up to 2% glycerol, all SP-LPGs respond linearly to changes in the surrounding RI. RI sensitivities are calculated by linear regression (solid lines) in this range. Each data point represents averaged data from triplicate experiments, with error bars denoting the standard deviation.

sensorgrams for the three SP-LPGs, while panels (b), (c), and (d) focus on the 13, 14.25, and 50 μm SP-LPGs, respectively. It is evident that the 50 μm SP-LPGs exhibits the poorest signal-to-noise ratio (S/N ratio) among the tested SP-LPGs. This is due to the smaller number of periods in this grating (80 periods over a 4 mm grating length) compared to the 13 μm ($\approx$308 periods) and 14.25 μm ($\approx$281 periods) SP-LPGs. The reduced number of periods significantly

Optics EXPRESS

Table 2. RI sensitivity, noise and resolution for the 13, 14.25 and 50 μm SP-LPGs. The simulated sensitivities are reported as bottom and top boundaries of the sensitivities of all the cladding modes in the family with *L* between 0 and 5 (as shown in Fig. 2).

Λ (μm)	Peak #	Sensitivity (Theoretical) [nm/RIU]	Sensitivity (Experimental) [nm/RIU]	Noise (σ) [nm]	RI Resolution (σ) [RIU]
13	1	207–247	227 ± 1.8		
13	2	235–279	248 ± 2.1		
13	**3**	**270–322**	**294 ± 3.7**	**1.0×10^{-4}**	**1.1×10^{-6}**
13	4	319–385	332 ± 3.7		
13	5	400–475	421 ± 11.0		
14.25	1	171–204	170 ± 1.3		
14.25	**2**	**188–223**	**198 ± 0.1**	**3.7×10^{-4}**	**5.5×10^{-6}**
14.25	3	206–246	206 ± 1.1		
14.25	4	230–274	225 ± 0.6		
50	**1**	**109–128**	**117 ± 1.5**	**6.3×10^{-3}**	**1.6×10^{-4}**

broadens the peak, making the estimation of its position noisier. The RI resolution is determined by calculating the RI change corresponding to a signal equal to the noise level, where the noise is represented by the standard deviation of the peak position fluctuations shown in Fig. S3(a).

The results of this analysis, including both theoretical and experimental RI sensitivity and resolution values, are presented in Table 2. For grating periods of 13 and 14.25 μm the experimental RI resolution is in the 10^{-6} range, which is within the required values reported in the literature for an optical biosensor [55].

As anticipated by theoretical simulations, the 13 μm SP-LPG demonstrates the highest RI sensitivity and best resolution among the tested devices. However, this period also exhibits the shortest linear response range, limiting its applications to scenarios where high sensitivity is required but a short linear range is acceptable. In contrast, the 14.25 μm SP-LPG provides a balanced compromise between sensitivity and linear response range, making it a strong candidate for biosensing applications. This balance is particularly valuable in the context of biological and chemical materials, which often exhibit inherent heterogeneity and therefore require versatile transducers. Finally, the 50 μm SP-LPG, although having the lowest sensitivity and resolution, offers the broadest linear response, making it suitable for applications where extended RI variations are expected. However, it is worth mentioning that if this device is intended to become a functionalized biosensor of a specific molecule, the most relevant refractive index range is close to the refractive index of water in the infrared range, which is around 1.318, as small concentrations will generate small changes of refractive index from that initial value. For this reason, we expect the first two periods (13 and 14.25 μm) to be the most suitable for a biosensor device.

5. Conclusions

In this study, we successfully fabricated, characterized, and theoretically modeled three SP-LPGs with different grating period lengths. Our investigation revealed that grating periods between 13 and 50 μm excite cladding modes that tend to cluster by *L* parity, generating a peak pattern characterized by two alternating families of peaks with odd and even *L* values. The cladding modes excited by these short periods also have a significantly higher sensitivity to RI changes with respect to typical LPGs. Specifically, the 13 μm SP-LPG exhibited the highest RI sensitivity, making it particularly suitable for applications requiring precise detection of minute changes in

Optics EXPRESS

the surrounding RI. However, this high sensitivity comes with the trade-off of a shorter linear detection range, limiting its applicability to scenarios where a wide dynamic range is not critical.

The intermediate 14.25 μm SP-LPGs presented the best compromise between sensitivity and linear response range, highlighting their versatility for a wide range of sensing applications, particularly in biosensing, where both sensitivity and linearity are crucial. Finally, the 50 μm SP-LPGs, with their longer grating period, demonstrated a more extensive linear response range but at the cost of reduced sensitivity and resolution. This characteristic makes them excellent candidates for applications that demand monitoring of broad RI variations, where a balance between sensitivity and range is necessary. This study demonstrates that SP-LPGs can be designed by adjusting the grating period to achieve desired trade-offs between sensitivity, resolution, and linearity. This systematic evaluation provides a practical guideline for tailoring SP-LPGs to application-specific requirements.

Our findings underscore the potential of SP-LPGs as highly adaptable and efficient RI sensors, with tunable properties tailored to specific application needs. By carefully selecting the grating period length, it is possible to optimize SP-LPGs for various practical scenarios, from high-sensitivity biochemical sensing to industrial process monitoring with a broader dynamic range. Future work should focus on refining the fabrication process to further enhance the performance and reliability of SP-LPGs, as well as exploring their integration into complex sensing systems for real-world applications. Overall, the demonstrated capabilities of SP-LPGs in this study pave the way for their expanded use in diverse fields, including medical diagnostics, environmental monitoring, and industrial process control, where precise and reliable sensing is fundamental. Although the results demonstrate the robustness and versatility of our SP-LPGs, certain aspects merit further exploration. For instance, optimizing the dynamic RI range for ultra-short period gratings and implementing strategies to compensate for temperature and strain effects are areas of ongoing investigation. Additionally, while this work focused on the optical characterization of bare SP-LPGs, efforts are underway to integrate them with surface functionalization protocols for selective biosensing applications, which would enable specific identification and quantification of target substances.

Funding. Ministero dell'Università e della Ricerca (IR0000036); Dipartimenti di Eccellenza.

Acknowledgments. This research was supported by the Department of Excellence in Robotics & AI, Scuola Superiore Sant'Anna, Piazza Martiri della Libertà 33, Pisa 56127, Italy. We acknowledge the financial support from project BRIEF "Biorobotics Research and Innovation Engineering Facilities" (Project identification code IR0000036) funded under the National Recovery and Resilience Plan (NRRP), Mission 4 Component 2 Investment 3.1 of Italian Ministry of University and Research funded by the European Union – NextGenerationEU. We also acknowledge Nitto Italia s.r.l. for providing the double-sided tape used in this work.

Disclosures. The authors declare that there are no conflicts of interest related to this article.

Data availability. Data underlying the results presented in this paper are not publicly available at this time but may be obtained from the authors upon reasonable request.

Supplemental document. See Supplement 1 for supporting content.

References

1. F. Baldini, M. Brenci, F. Chiavaioli, *et al.*, "Optical fibre gratings as tools for chemical and biochemical sensing," Anal. Bioanal. Chem. **402**(1), 109–116 (2012).
2. F. Chiavaioli, F. Baldini, S. Tombelli, *et al.*, "Biosensing with optical fiber gratings," Nanophotonics **6**(4), 663–679 (2017).
3. X. Zhang, W. Ji, S. Y. H. Kit, *et al.*, "A novel structure of microfiber-based sensor for onsite/insitu detection of heavy metal ions," in *Conference on Lasers and Electro-Optics/Pacific Rim* (Optica Publishing Group, 2018), paper Th3L–1.
4. R. Rohan, K. Venkadeshwaran, and P. Ranjan, "Recent advancements of fiber bragg grating sensors in biomedical application: a review," J. Opt. **53**(1), 282–293 (2024).
5. A. D. Kersey, M. A. Davis, H. J. Patrick, *et al.*, "Fiber grating sensors," J. Lightwave Technol. **15**(8), 1442–1463 (1997).
6. V. Bhatia and A. M. Vengsarkar, "Optical fiber long-period grating sensors," Opt. Lett. **21**(9), 692–694 (1996).

Optics EXPRESS

7. V. Bhatia, *Properties and sensing applications of long-period gratings* (Virginia Polytechnic Institute and State University, 1996).
8. J. Ran, Y. Chen, G. Wang, *et al.*, "Mechanically induced long-period fiber gratings and applications," in *Photonics*, vol. 11 (MDPI, 2024), p. 223.
9. R. M. A. Ayaz, Y. Uysalli, B. Morova, *et al.*, "Linear cavity tapered fiber sensor using mode-tracking phase-shift cavity ring-down spectroscopy," J. Opt. Soc. Am. B **37**(6), 1707–1713 (2020).
10. K. Zhou, X. Chen, L. Zhang, *et al.*, "Implementation of optical chemsensors based on hf-etched fibre bragg grating structures," Meas. Sci. Technol. **17**(5), 1140–1145 (2006).
11. A. Ruskuc, P. Koehler, M. A. Weber, *et al.*, "Excitation of higher-order modes in optofluidic photonic crystal fiber," Opt. Express **26**(23), 30245–30254 (2018).
12. W. W. Morey, G. Meltz, and W. H. Glenn, "Fiber optic Bragg grating sensors," in *Fiber optic and laser sensors VII*, vol. 1169 (SPIE, 1990), pp. 98–107.
13. F. Esposito, A. Srivastava, L. Sansone, *et al.*, "Label-free biosensors based on long period fiber gratings: a review," IEEE Sens. J. **21**(11), 12692–12705 (2021).
14. X. Shu, T. Allsop, B. Gwandu, *et al.*, "High-temperature sensitivity of long-period gratings in b-ge codoped fiber," IEEE Photonics Technol. Lett. **13**(8), 818–820 (2001).
15. R. Wang, Z. Ren, X. Kong, *et al.*, "Graphene-assisted high-precision temperature sensing by long-period fiber gratings," J. Phys. D: Appl. Phys. **53**(6), 065104 (2020).
16. Y. Zhang, P. Jiang, D. Qiao, *et al.*, "Sensing characteristics of long period grating by writing directly in smf-28 based on 800 nm femtosecond laser pulses," Opt. Laser Technol. **121**, 105839 (2020).
17. I. Del Villar, O. Fuentes, F. Chiavaioli, *et al.*, "Optimized strain long-period fiber grating (lpfg) sensors operating at the dispersion turning point," J. Lightwave Technol. **36**(11), 2240–2247 (2018).
18. S. K. A. K. Bey, T. Sun, and K. T. Grattan, "Simultaneous measurement of temperature and strain with long period grating pairs using low resolution detection," Sens. Actuators, A **144**(1), 83–89 (2008).
19. T. Allsop, M. Dubov, A. Martínez, *et al.*, "Bending characteristics of fiber long-period gratings with cladding index modified by femtosecond laser," J. Lightwave Technol. **24**(8), 3147–3154 (2006).
20. K. Ren, L. Ren, J. Liang, *et al.*, "Highly strain and bending sensitive microtapered long-period fiber gratings," IEEE Photonics Technol. Lett. **29**(13), 1085–1088 (2017).
21. R. Subramanian, C. Zhu, H. Zhao, *et al.*, "Torsion, strain, and temperature sensor based on helical long-period fiber gratings," IEEE Photonics Technol. Lett. **30**(4), 327–330 (2018).
22. X. Shu, L. Zhang, and I. Bennion, "Sensitivity characteristics of long-period fiber gratings," J. Lightwave Technol. **20**(2), 255–266 (2002).
23. F. Esposito, "Chemical sensors based on long period fiber gratings: A review," Res. Opt. **5**, 100196 (2021).
24. L. Chen, Y. Ma, C. Jiang, *et al.*, "High-sensitive refractive index sensor based on the long-period gratings inscribed in the tapered fiber at dispersion turning point," Opt. Commun. **569**, 130798 (2024).
25. Y. Zhuo, P. Ma, P. Jiao, *et al.*, "Application of long-period fiber grating sensors in structural health monitoring: A review," CivilEng. **5**(3), 559–575 (2024).
26. A. Stăncălie, D. Sporea, D. Neguţ, *et al.*, "Long period gratings in unconventional fibers for possible use as radiation dosimeter in high-dose applications," Sens. Actuators, A **271**, 223–229 (2018).
27. S. Korposh, R. Selyanchyn, S. James, *et al.*, "Identification and quality assessment of beverages using a long period grating fibre-optic sensor modified with a mesoporous thin film," Sens. Bio-Sensing Res. **1**, 26–33 (2014).
28. G. Quero, M. Consales, R. Severino, *et al.*, "High sensitive long period fiber grating biosensor for cancer biomarker detection," in *HEALTHINF*, (2016), pp. 561–569.
29. G. Quero, S. Zuppolini, M. Consales, *et al.*, "Long period fiber grating working in reflection mode as valuable biosensing platform for the detection of drug resistant bacteria," Sens. Actuators, B **230**, 510–520 (2016).
30. C. Trono, "Long period fiber grating-based biosensing: recent trends and future perspectives," TrAC Trends Anal. Chem. **179**, 117875 (2024).
31. X.-W. Zhao and Q. Wang, "Mini review: Recent advances in long period fiber grating biological and chemical sensors," Instrum. Sci. & Technol. **47**(2), 140–169 (2019).
32. M. Peng, Z. Lu, Y. Tang, *et al.*, "Femtosecond laser direct writing of long period fiber grating sensor with high refractive index sensitivity," Opt. Fiber Technol. **81**, 103511 (2023).
33. W. Bu, X. Wang, Z. Wu, *et al.*, "Temperature-insensitive refractive index sensor based on high-order-resonance short-line long-period fiber grating," Sens. Actuators, A **360**, 114540 (2023).
34. J. Huang, X. Lan, A. Kaur, *et al.*, "Temperature compensated refractometer based on a cascaded sms/lpfg fiber structure," Sens. Actuators, B **198**, 384–387 (2014).
35. Z.-M. Zheng, Y.-S. Yu, X.-Y. Zhang, *et al.*, "Femtosecond laser inscribed small-period long-period fiber gratings with dual-parameter sensing," IEEE Sens. J. **18**(3), 1100–1103 (2018).
36. J. Wang, F. Shen, X. Shu, *et al.*, "Line by line inscribed small period long period grating for wide range refractive index sensing," Opt. Commun. **508**, 127821 (2022).
37. R. Zhao, H. Liu, and X. Shu, "Femtosecond laser-inscribed off-axis high-order mode long-period grating for independent sensing of curvature and temperature," Opt. Express **30**(21), 37697–37710 (2022).
38. F. Shen, C. Wang, Z. Sun, *et al.*, "Small-period long-period fiber grating with improved refractive index sensitivity and dual-parameter sensing ability," Opt. Lett. **42**(2), 199–202 (2017).

Optics EXPRESS

39. N. L. Mahgoob and A. A. Al-Dergazly, "Fabrication long period fiber bragg grating by using co_2 laser," J. Opt., pp. 1–6 (2025).
40. J. Cai, H. Liu, Y. Liu, *et al.*, "A small-period long-period fiber grating biosensor based on immobilization of concanavalin a on polydopamine nanospheres for simultaneous detection of d-glucose and temperature," Measurement **242**, 115877 (2025).
41. H. Liu, J. Cai, L. Zhang, *et al.*, "Femtosecond laser inscribed small-period long-period fiber grating coated with a nano-assembled polyelectrolyte film for independent sensing of ammonia gas and temperature," Sens. Actuators, B **423**, 136860 (2025).
42. X. Li, B. Xie, M. Wu, *et al.*, "Visible-to-near-infrared optical properties of protein, lipid and carbohydrate in both solid and solution state at room temperature," J. Quant. Spectrosc. Radiat. Transf. **259**, 107410 (2021).
43. C. Massaroni, D. L. Presti, C. Losquadro, *et al.*, "Multi-sensitive fbg-based needle for both relative humidity and breathing rate monitoring," in *International Symposium on Medical Measurements and Applications* (IEEE, 2018), pp. 1–6.
44. Y. Yan, Z. Gu, Y. Wang, *et al.*, "Design and simulation of reflective fiber grating sensor for simultaneous monitoring of ctd in marine environment," J. Opt., pp. 1–12 (2024).
45. C. Hu, X. Guo, C. Jiang, *et al.*, "Long-period fiber grating based on micro-holes-filled pdms for temperature and pressure measurement," Infrared Phys. & Technol. **136**, 105065 (2024).
46. R. Falate, J. L. Fabris, M. Muller, *et al.*, "Long period grating sensor to monitor fuel quality," Asian J. Phys. **12**, 205 (2003).
47. C. Yeh and G. Lindgren, "Computing the propagation characteristics of radially stratified fibers: an efficient method," Appl. Opt. **16**(2), 483–493 (1977).
48. S. R. Dods, "Fiber vector modesolver-improvements to the efficient 4× 4 matrix method," in *Integrated Photonics Research and Applications*, (Optica Publishing Group, 2006), paper ITuF5.
49. I. H. Malitson, "Interspecimen comparison of the refractive index of fused silica," J. Opt. Soc. Am. **55**(10), 1205–1209 (1965).
50. G. M. Hale and M. R. Querry, "Optical constants of water in the 200-nm to 200-μm wavelength region," Appl. Opt. **12**(3), 555–563 (1973).
51. T. Erdogan, "Cladding-mode resonances in short-and long-period fiber grating filters," J. Opt. Soc. Am. A **14**(8), 1760–1773 (1997).
52. J. E. Saunders, C. Sanders, H. Chen, *et al.*, "Refractive indices of common solvents and solutions at 1550 nm," Appl. Opt. **55**(4), 947–953 (2016).
53. R. Funari, K.-Y. Chu, and A. Q. Shen, "Detection of antibodies against sars-cov-2 spike protein by gold nanospikes in an opto-microfluidic chip," Biosens. Bioelectron. **169**, 112578 (2020).
54. R. Funari, K.-Y. Chu, and A. Q. Shen, "Multiplexed opto-microfluidic biosensing: Advanced platform for prostate cancer detection," ACS Sens. **9**(5), 2596–2604 (2024).
55. M. C. Estevez, M. Alvarez, and L. M. Lechuga, "Integrated optical devices for lab-on-a-chip biosensing applications," Laser Photonics Rev. **6**(4), 463–487 (2012).